Aerosol Res., 4, 265–277, 2026
https://doi.org/10.5194/ar-4-265-2026

AEROSOL Research
Open Access

Nascent titanium-/silicon-containing particle formation in corona-discharge-assisted combustion

Chanakya Bagya Ramesh[1], **Frank Daoru Han**[2], **and Yang Wang**[1]

[1]Department of Chemical, Environmental, and Materials Engineering, University of Miami, Coral Gables, Florida, 33146, United States
[2]Department of Mechanical and Aerospace Engineering, Missouri University of Science and Technology, Rolla, Missouri, 65409, United States

Correspondence: Yang Wang (yangwang@miami.com)

Received: 19 December 2025 – Discussion started: 2 January 2026
Revised: 15 March 2026 – Accepted: 16 April 2026 – Published: 1 July 2026

Abstract. Adding plasmas to a flame has been shown to introduce high concentrations of charges, ions, and radicals to the said flame. This technique of adding plasma to a flame is called plasma-assisted combustion (PAC), and this addition has been shown to make a flame more stable and efficient. At the same time, PAC has also been shown to alter particle formation during combustion. Here, we investigate the effect of a high-frequency (~ 21 kHz) alternating current (AC) corona discharge on particle formation and growth in a premixed flame, especially at the initial stages (with particle sizes below 10 nm). We first examined the mobility size distribution of ions generated from non-plasma combustion and corona-discharge-assisted combustion. The mobility size for positive ions does not change with the introduction of plasma. However, the negative ions change towards a larger size, likely due to different ion chemistry from plasma. We then introduced corona discharge with varying powers into the flame that contains titanium isopropoxide (TTIP) or tetraethyl orthosilicate (TEOS) and obtained the size distribution of the synthesized nanoparticles. For the precursor feed rates used in this study (TTIP: 9.6–48 mg h^{-1}, TEOS: 60–100 mg h^{-1}), we found that particle growth is suppressed by the corona discharge under relatively higher precursor feed rates (above ~ 29 mg h^{-1} for TTIP and above ~ 80 mg h^{-1} for TEOS). The mobility diameter is suppressed by up to 12 % for TTIP and by up to 20 % for TEOS. We further used different charging models to examine the impact of plasma on particle formation. In the case of higher precursor feed rates, the incipient particle concentration is high within the flame region. As higher number of charges accumulated on particles from negative-charge carriers (including electrons and negative ions) than positive ions, the particles are preferentially charged negative. Such preferential charging results in particle–particle repulsion, which suppresses coagulation particle growth. The findings of this study can guide nanoparticle synthesis and particulate matter control using PAC.

1 Introduction

Nanomaterial production is a significant global industry, valued at USD 16.3 billion in 2025 (Nanomaterials Market Size And Share Report, 2026). Recent advancements in battery technology, drug delivery systems, and energy conversion have driven a growing demand for nanomaterials, with a projected compound annual growth rate (CAGR) of 15 % over the next 6 years (Nanomaterials Market Size And Share Report, 2025). Combustion synthesis is considered one of the most effective methods for producing nanomaterials (Li et al., 2016), and a substantial portion of current nanomaterial production relies on combustion-based processes. These processes employ aerosol-focused technologies to control and optimize production, leveraging the bottom-up approach at the nanometer scale. Due to the rapid formation of aerosols within the coupled thermal and flow fields in combustion synthesis, the properties of the synthesized nanomaterials are

sensitive to flame instability and fuel incomplete combustion, which may deteriorate the quality of the synthesized nanomaterials (Gröhn et al., 2014; Rittler et al., 2017; Serrano-Bayona et al., 2023).

One technology proposed to reduce flame instability and promote fuel combustion is plasma-assisted combustion (PAC). PAC introduces plasmas into combustion, and studies have shown that this makes the flame more stable (Bradley and Nasser, 1984; Galley et al., 2005; Liao and Zhao, 2018; Vincent-Randonnier et al., 2007) and efficient (Galley et al., 2005; De Giorgi et al., 2017; Rosocha et al., 2004) while also reducing emissions (Cha et al., 2005). These improvements have been observed across various types of non-equilibrium plasmas, including a corona discharge (Bradley and Nasser, 1984), nanosecond repetitive-pulse discharge (Galley et al., 2005), dielectric barrier discharge (Cha et al., 2005; De Giorgi et al., 2017; Rosocha et al., 2004), and microwave discharge (Ehn et al., 2017). The benefits have been attributed to the high concentration of charge carriers and radicals generated by the plasma (De Giorgi et al., 2017), which influence both the chemical reactions responsible for forming nascent particles and the growth of these particles during combustion. Since the properties of these charge carriers and radicals can be altered by changing the properties of plasma, PAC provides an opportunity to engineer the synthesis of nanomaterials. Apart from these positive effects, the introduction of electric fields to flames at sub-breakdown voltages may also produce adverse effects. Under such conditions, both DC and AC electric fields have been reported to induce flame instability by displacing the flame toward the grounded electrode (Ren et al., 2018; Tang et al., 2022). For AC electric fields, instabilities occur primarily at low frequencies (< 10 Hz) (Tang et al., 2022), whereas at higher frequencies (50–500 Hz), they have been observed to increase flame temperature, suggesting a higher Damköhler number and greater stability (Gan et al., 2015). While studies have shown that plasma suppresses the growth of soot particles (Cha et al., 2005; Ohisa et al., 1999; Su et al., 2018), very few studies have looked at the effect of plasma on the combustion synthesis of inorganic particles. Furthermore, there has been no in situ diagnostic investigation of aerosol formation during PAC, highlighting the gap in current research.

Particle formation in combustion systems has been widely studied, and it is well established that this process occurs in several stages, including nucleation, coagulation, condensation, and sintering (Carbone et al., 2008, 2021; Pratsinis, 1998; Wang et al., 2017b, c). The formation and subsequent growth of particles are strongly influenced by interactions between particles, charged carriers, and the surrounding electric field. Flames, being weak plasma systems themselves, contain relatively high concentrations of charge carriers, such as ions and electrons (Fialkov, 1997). Several studies have sought to exert a greater influence on the particle–charge carrier interaction by applying external electric fields to manipulate the movement of charge carriers (Altendorfner et al., 2011; Belhi et al., 2010; Kammler et al., 2003; Saito et al., 1999; Xiong et al., 2017; Zhao et al., 2008). By introducing plasmas into flames, PAC will significantly enhance particle interactions with charged carriers and electric fields. As opposed to moving charge carriers in a flame using electric fields, introducing plasma into a flame allows for more extensive modifications of reaction kinetics (Ju and Sun, 2015a, b). Introducing plasma into a flame will significantly increase the concentration of charges and radicals. Depending on the type of plasma, the electron concentration can reach up to 10^{23} m^{-3}, with electron energies ranging from 0.8 to 10 eV. In addition to high-energy electrons, there is also high concentration of radicals such as NO, O_3, O, H, and OH (Ju and Sun, 2015a). Although each of these components play a role in enhancing the flame, the most important component is the high-energy electron due to its ability to initiate or alter reactions. Li et al. (2019) discovered that in a corona discharge, the electron temperature around the electrode can increase by 350 %, and the concentration of plasma-related species (including radicals and charge carriers) can increase by 400 %. Ohisa et al. (1999) show that these electrons and charged species are generated on the tip/edge of the electrodes, which are placed outside the high-temperature region, and how they are introduced into the flame depends on the type of power source used to generate the discharge. The same study shows that a difference in cation concentrations when using a DC power source is 10 times higher than it is when using an AC power source. This suggests that when a DC power source is used, the charged species are introduced to the flame via the ionic wind, and in the case of an AC power source, the charged species enter the flame predominantly via diffusion (Ohisa et al., 1999). Though the ionic wind effects might still be present in the case of an AC power source, they are not as dominant as the ionic wind effects in the case of a DC power source. This difference in the concentration of charged species can lead to the plasma having different effects on particle formation and growth in combustion systems.

Although studies have investigated PAC on its role in enhancing flame stability and efficiency, only a few have focused specifically on particle formation and growth. Vemury and Pratsinis (1995) examined the TiO_2 particles produced in a DC corona-discharge-assisted diffusion flame reactor. They reported that the corona discharge reduces the particle residence time in the high-temperature region due to ionic wind effects, reducing the particle diameter. Similarly, Ohisa et al. (1999) applied DC and AC corona discharges to a sooting propane turbulent diffusion flame and reported a significant reduction in soot. This reduction was attributed to the charging of incipient soot particles and decreased concentration of ions like $C_3H_3^+$, which act as precursors in the ionic mechanism of soot formation. Despite these findings, further research is needed to obtain a more mechanistic and comprehensive understanding of particle formation and growth in PAC under different plasma and flame configurations. This study aims to investigate the impact of introducing

corona discharge into a flame on the size distribution of inorganic particles. A high-voltage AC power source is used to generate corona discharges of varying powers across a premixed methane–air flame. The flame is fed with Ti- and Si-based precursors to generate Ti-containing or Si-containing nanoparticles. In this study, we use a high-resolution differential mobility analyzer (HRDMA) combined with an electrometer to obtain the size distribution of particles (Fernández de la Mora and Kozlowski, 2013) in the size range of 1 to 10 nm. We examined the effect of corona discharge on the size distribution of Ti-containing and Si-containing particles under varying plasma powers, precursor feed rates, and for both positively and negatively charged particles. We further used different charging models to examine the impact of plasma on particle formation. The methods and results of this study can be used to design nanomaterials synthesis platforms using PAC.

2 Methods

2.1 Flame and particle analysis

The schematic diagram of the combustion system used is shown in Fig. 1a, which is similar to that presented in Bagya Ramesh and Wang (2024). We used a premixed flame sustained above a tube burner. The burner was built using two 316 L stainless steel tubes with outer diameters of 6.35 and 12.7 mm, which were placed concentrically. A stream of N_2 at a flow rate of $0.6\,\mathrm{L\,min^{-1}}$ was introduced through the space between the two tubes as a sheath. CH_4 and O_2 were introduced to the inner tube at flow rates of 0.09 and $0.18\,\mathrm{L\,min^{-1}}$, respectively, to provide a stoichiometric flame. Particle synthesis precursors, titanium isopropoxide (TTIP) or tetraethyl orthosilicate (TEOS), were added to the gas mixture to generate Ti-containing and Si-containing particles. We chose to study the formation of Ti-containing and Si-containing particles, as they are among the most important inorganic oxides produced by combustion, which are used extensively in paints (Braun et al., 1992), catalysts (Kim et al., 2011; Niu et al., 2014), solar cells (Thimsen et al., 2008), carbon-based product manufacturing (Spicer et al., 1998), and drug delivery systems (Alavi et al., 2022). The precursors are liquid and were introduced into the reactant stream in the gaseous phase by bubbling N_2 through their respective liquid media. We could introduce different amounts of precursors by varying the flow rate of N_2 passed through the precursor (calibrated using a bubble flow meter, Sensidyne Gilian Gilibrator) and the temperature of the precursor liquid. The amount of TTIP and TEOS introduced was calculated by obtaining their saturation vapor pressures from Eqs. (1) and (2), respectively (Jang, 1999; Siefering and Griffin, 1990).

$$\log_{10}\left(P_{\mathrm{eq}}\right) = 9.837 - \frac{3193.7}{T} \tag{1}$$

$$\ln P = 19.3 - \frac{5555}{T} \tag{2}$$

We used precursor feed rates of 9.6, 19.2, 28.7, 38.4, and $48\,\mathrm{mg\,h^{-1}}$ for TTIP and 60, 80, and $100\,\mathrm{mg\,h^{-1}}$ for TEOS when synthesizing Ti-containing and Si-containing particles. We obtained the above feed rates by introducing N_2 through TTIP at a flow rate of 0.1, 0.2, 0.3, 0.4, and $0.5\,\mathrm{L\,min^{-1}}$. Similarly, for TEOS, we used an N_2 flow rate of 0.03, 0.04, and $0.05\,\mathrm{L\,min^{-1}}$. Additional N_2 was introduced to the flame through the inner tube so that the O_2 and N_2 molar ratio was maintained at 1 : 3.76, simulating the air composition. To check if the flame was altered by the consumption of oxygen towards the oxidation of TTIP and TEOS, we calculated the flame equivalence ratio with precursors at their highest feed rates. If the equivalence ratio (ϕ), the fuel-to-oxidizer ratio to the stoichiometric fuel-to-oxidizer ratio, shifts significantly towards fuel-rich conditions ($\phi > 1$), we would see the shift reflected in a significant change in flame temperature. For flame temperature measurement, we used a type S thermocouple (Pt – 10 % Rh) with an exposed uncoated spherical bead of diameter 0.7 mm. In Fig. 1b, we can see the temperature profile, which takes into account the radiative heat losses on the thermocouple bead surface. Based on the highest feed rate of both precursors, $48\,\mathrm{mg\,h^{-1}}$ for TTIP and $100\,\mathrm{mg\,h^{-1}}$ for TEOS, complete oxidation of TTIP would make the flame $\sim 0.7\,\%$ fuel rich relative to a stoichiometric flame, while TEOS would make the flame $\sim 1.3\,\%$ fuel rich. Because the flame remains close to stoichiometric conditions, there is little to no change in flame temperature, as shown in Fig. 1b. We should note that there might be trace amounts of carbon on generated particles due to slightly fuel-rich conditions. The particles formed from the flame are extracted and studied using a hole-in-a-tube (HiaT)-type dilution sampling probe (Zhao et al., 2003), SEADM HRDMA, and a TSI 3068A electrometer. Only the DMA cell in HRDMA was purchased from SEADM, while the rest of the components were built in house as described in Wang et al. (2014). The HiaT dilution sampling probe is 1/4 in. straight stainless steel with a 0.1 mm diameter orifice. The sampling probe is operated with zero air as the diluent, which is generated by a HEPA filter. Due to dilution, the temperature after mixing is sufficiently low that it can reduce further oxidation by air in the dilution probe. We also measured the size distribution of particles to ensure that the normalized size distributions do not change as we further increase the dilution ratios, meaning that further reactions and particle dynamics are quenches in the sampling probe (Wang, 2017; Zhao et al., 2003). Two streams of diluent air are provided to the sampling probe, one upstream (diluent air) and one downstream (secondary air) of the aerosol sampling inlet. The aerosol flow rate at the probe inlet above the flame is controlled by controlling the upstream and downstream airflow. The diluent air and secondary air used for the dilution sampling probe are supplied at a rate of ~ 31 and $2\,\mathrm{L\,min^{-1}}$.

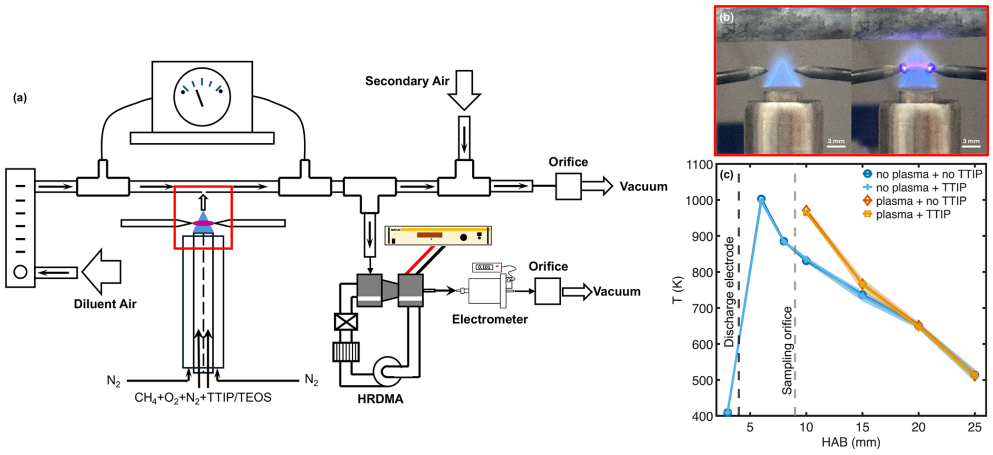

Figure 1. **(a)** Schematic of the experimental apparatus, with the red box highlighting the flame and corona discharge region. **(b)** Image of flame with and without a corona discharge in the highlighted region. **(c)** Temperature profile of flames under different plasma and synthesis precursor conditions. The feed rate of TTIP is 19 mg h^{-1} for the temperature profile measurement, and the plasma power is 125 W.

Using the method in Zhao et al. (2003), we calculated the dilution ratio for this study, which is 152 after accounting for the thermal expansion of air. A single set of flow conditions was used for all experiments. Flow rates in the dilution system were held constant to keep the dilution ratio and sampling conditions consistent across cases. The above ratio is a product of the dilution due to flow mixing and thermal expansion. Dilution due to flow mixing was obtained by measuring the ambient particle concentration with and without dilution using a TSI model 3750 condensation particle counter and was found to be 45.3. Dilution due to thermal expansion was 3.36 from the ratio of aerosol sample temperature (1003 K) to that of dilution air (298 K). For our experiments, particles were sampled using a 1/4 in. copper tube with a length of 0.88 m with 5.85 L min^{-1} of flow pass-through. The number concentration detected by the electrometer was of the order of 10^5 cm^{-3}. To correct the number concentration of the measured charged particles, we performed data inversion as described in our previous work (Bagya Ramesh and Wang, 2024). The data inversion, which accounts for diffusional and penetration losses, increased the number concentration of our measured size distributions to the order of 10^{10} cm^{-3}. This result is expected, given the sub-10 nm particle size range being sampled. The HRDMA was operated in series with a TSI 3068A electrometer. HRDMA used a sheath flow of 277.5 L min^{-1} and a sample flow rate of 5.85 L min^{-1}. The voltage of the central electrode was scanned from 0 to 5000 V to obtain mobility diameters of particles up to a size of 8 nm. We should note that throughout this paper, the term particle size refers specifically to the mobility size. Mobility size differs from the actual particle diameter, as it is determined by the balance between drag forces and electrostatic forces acting on the particle in an electric field. The mobility size can be related to the physical size, aerodynamic size, or the volumetric size of the aerosol particles (Larriba et al., 2011). However, these conversions require knowledge on the shape and density of the particles. The HRDMA was calibrated using monodisperse tetra-alkyl ammonium halide ions (Ude and De La Mora, 2005), and we can convert mobility to mobility size based on the following equation:

$$Z = Cne/3\pi\mu D_p. \quad (3)$$

In Eq. (3), C is the Cunningham slip correction factor, n is the number of charges on the particle, e is the electronic charge, μ is the air viscosity, and D_p is the mobility size.

To generate the corona discharge, we used two tungsten electrodes placed 6 mm apart and 3 mm above the tube burner. The electrodes were provided by Thermo Scientific as 2 mm diameter Tungsten rods of purity 99.95 % (metals basis). The high purity of the material ensured minimal corrosion even after using them for several hours. The tips of the electrodes were sharpened to increase the intensity of the electric field and facilitate gas breakdown. A high-voltage, high-frequency AC power supply (PVM400DELUX, HVC Capacitor Manufacturing Co., Ltd) was used as the power source. This AC power source has a variable output from 1 to 15 KV and from 20 to 50 kHz. For the experiments conducted in this study, we examined the corona discharge generated from this power source under two different operating conditions. One operating condition corresponds to the onset of the corona discharge (1.9 kV, 58.5 mA, 21.6 kHz), and the other operating condition corresponds to the maximum power of the power supply (1.8 kV, 131.6 mA, 20.4 kHz). The major difference between the two conditions is the current through plasma or the power of the plasma (56 and 125 W). Since the power source is high-frequency AC, ionic wind effects are minimized and can be ignored. Flame temperature was also measured in the presence of a corona discharge (at 125 W). To minimize plasma interference, the thermocouple probe was positioned at least 6 mm from the discharge electrodes.

Table 1. Experimental plan for this study.

Task	Precursor	Corona discharge power
1	–	–
2	–	56 and 125 W
3	TTIP (9.6–48 mg h^{-1})	–
4	TTIP (9.6–48 mg h^{-1})	56 and 125 W
5	TEOS (60–100 mg h^{-1})	–
6	TEOS (60–100 mg h^{-1})	125 W

Introducing the corona discharge increased flame temperature, an unexpected result given the non-thermal nature of the corona discharge plasma. This effect can be attributed to elongation of the flame reaction zone observed in our experiment, which extended the high-temperature region. The resulting temperature rise may also influence particle formation and growth downstream. The experimental conditions used in this study are summarized in Table 1.

2.2 Estimating charging characteristics

The particle charging characteristics of plasma ions and electrons were calculated to understand the role of charging in particle growth within such systems. We analyzed the diffusion and field charging effects of ions sampled under two conditions: flame only and PAC with a plasma power of 125 W. The diffusion charging effects were determined using Eq. (4), while the field charging effects were calculated using Eq. (5) (Liu and Yeh, 1968; Friedlander, 2000).

$$n_{\text{diff}} = \left(akT/\epsilon^2\right) \ln\left(1 + \pi\epsilon^2 caN_0 t/kT\right) \tag{4}$$

$$n_{\text{fld}} = n_s \pi N_0 \epsilon Zt/(\pi N_0 \epsilon Zt + 1) \tag{5}$$

In Eq. (4), a is the particle radius, c is the thermal speed of ions, N_0 is the concentration of ions far away from the particle, ϵ is the elementary unit charge, k is Boltzmann's constant, t is the exposure time of the particle to unipolar ions, n_{diff} is the charge acquired by the particle due to diffusion charging, n_{fld} is the charge acquired by the particle due to field charging, and T is the temperature in K. The transport time of aerosols from the sampling probe inlet to the HRDMA inlet is 86.3 ms. During transport, diffusion charging remains active in the diluted flow. Field charging, however, is considered only while the particles are between the post-flame region and probe inlet, corresponding to the exposure time, whereas diffusion charging is considered for the entire period between the post-flame region and the HRDMA inlet, corresponding to the combined exposure time and transport time in the sampling line. We calculate the charge estimates at 20 different logarithmically spaced particle radii, a, ranging from 0.1 to 10 nm. The thermal speed of ions, c, was calculated using Eq. (6), which stems from the Maxwell–Boltzmann distribution law. In Eq. (6), m is the mass of the ion estimated using the mobility of ions measured from HRDMA and based on the mass–mobility relationship presented by Kilpatrick (Mäkelä et al., 1996). N_0 is the concentration of ions measured in different flame and plasma conditions without precursors, as shown in Fig. 2. The value of T is taken as 1003 K, the peak temperature measured.

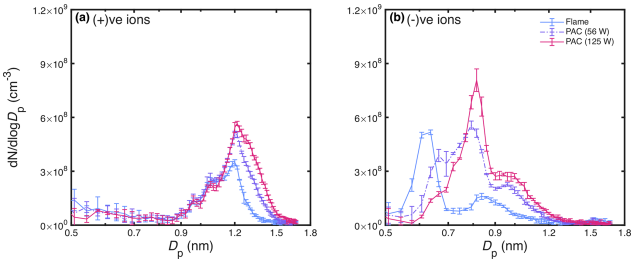

Figure 2. **(a)** The size distribution of positive ions under a flame with and without a corona discharge. **(b)** The size distribution of negative ions under a flame with and without a corona discharge. Both panels show the effect of corona discharge at a power of 56 and 125 W on the ionic size distribution. Error bars denote the standard deviation.

$$c = \sqrt[2]{8kT/\pi m} \tag{6}$$

In Eq. (5), Z is the mobility diameter, and n_s is the saturation charge. Although not directly used in Eq. (5), the value of the particle's dielectric constant (K) is required to calculate n_s. The saturation charge is calculated using Eq. (7), where E_0 is the intensity of the applied electric field. E_0 is calculated from Eqs. (8) and (9), where V_{peak} is the peak voltage of the AC power source used for both plasma conditions, 56 and 125 W, used in this study, and d is the distance between the discharge electrodes. V_{peak} for our experiments is 1.9 KV, and d for all experimental conditions is fixed at 3.87 mm.

$$n_s = \left\{1 + 2\left[(K-1)/(K+2)\right]\right\}\left(E_0 a^2/\epsilon\right) \tag{7}$$

$$V_{\text{rms}} = V_{\text{peak}}/\sqrt{2} \tag{8}$$

$$E_0 = V_{\text{rms}}/d \tag{9}$$

We present here only the key equations used to calculate charge accumulation on particles, and the detailed steps for this calculation can be found elsewhere (Liu and Yeh, 1968; Friedlander, 2000). Assuming that the particles were mostly TiO_2 and SiO_2, the dielectric constants for these particles were taken as 30 and 3.9, respectively. All parameters used in Eqs. (4) and (5) were expressed in SI units. To estimate the exposure time of particles to ions, we calculated the gas flow velocity and the time that particles remain between the post-flame region before entering the sampling probe inlet. The volumetric flow rate of the flame was calculated from CH_4, O_2, and N_2 feed rates to be 1.578×10^{-5} m^3 s^{-1}. Dividing the volumetric flow rate by the cross-sectional area of tube

burner gave us a flow velocity of 0.962 m s^{-1}. The particles were assumed to be exposed to the ions only for the duration that they spent between the post-flame region and the sampling probe's inlet. By measuring optically using the images shown in Fig. 1b, the flame height was found to be 4.38 mm. In the flame-only condition, this distance was 3.26 mm, giving an exposure time of 3.9 ms. For the flame with a plasma condition, this distance was 2 mm, giving an exposure time of 2.08 ms. These calculations assume that only neutral particles are charged through field charging.

3 Results and discussion

3.1 Ions of flames vs. plasma

Figure 2 shows the size distributions of positive and negative ions measured in the flame with and without a corona discharge. The size distributions are measured in the absence of particle-forming precursors. From Fig. 2b, the negative ions exhibit bimodal peaks at 0.6 and 0.8 nm for the flame without the corona discharge condition, whereas for the same condition, the positive ions display a broader unimodal peak at 1.2 nm (Fig. 2a). The size distributions of flame-generated ions are similar to those reported in a previous study (Bagya Ramesh and Wang, 2024), which are dominated by charge carriers below 2 nm. After introducing the corona discharge into the flame, the positive-ion size distribution does not change significantly with regard to size (Fig. 2a). The peak size for the positive ions stays at around 1.2 nm under corona discharge powers of 56 and 125 W. However, there is a significant increase in ion concentration, with an increase of 45 % and 62 % for corona discharge powers of 56 and 125 W. The relative consistency of the mobility sizes for positive ions with and without the corona discharge implies that positive-ionic species are similar under all three conditions. At the same time, the increase in concentration indicates that the corona discharge enhances the rate of reactions responsible for forming these ions from both combustion and corona discharge. However, the ion concentrations under corona discharge do not scale with the plasma power.

Regarding the negative-ion size distributions, in a flame assisted by a corona discharge at 56 W, the peak at 0.6 nm slightly diminished, while the peak at 0.8 nm was enhanced (Fig. 2b). At the same time, we see a peak emerge at 1.0 nm. This trend continues when the corona discharge power increases to 125 W, with a more substantial peak at 0.8 nm and 1.0 nm. This suggests that the introduction of a corona discharge promotes reactions that generate ions with a mobility diameter of 0.8 nm in the flame without plasma (Fig. 2b).

3.2 Influence of corona discharge on size distribution of particles

Figures 3 and 4 show the size distribution of Ti-containing particles forming under different TTIP feed rates and different corona discharge conditions. Overall, as the feed rate of TTIP increases from 9.6 to 48 mg h^{-1}, we observe an increase in the concentration of Ti-containing particles, which results in particles growing to larger sizes by coagulation. Compared to the flame without plasma, the size distribution of particles formed with plasma shifts toward larger sizes under low precursor concentrations ($\leq$ 19.2 mg h^{-1}) and toward smaller sizes under high precursor concentrations ($\geq$ 28.7 mg h^{-1}).

Under the lower TTIP feed rates of 9.6 mg h^{-1} (Fig. 3b) and 19.2 mg h^{-1} (Fig. 3c), in a corona-discharge-assisted combustion atmosphere, we observe that particle concentration is promoted compared to the flame without plasma. A similar effect appears for the size distribution of negatively charged clusters, as seen in the plots of Fig. 4b and c. For positively charged clusters, the concentration of the flame-generated particles under 125 W plasma increases by 86 % and 150 % for the feed rate of 9.6 and 19.2 mg h^{-1}, respectively, compared to the condition without plasma (Fig. 3b and c). The increase in particle concentration also promotes the coagulation growth of the particles, where the particle size from a feed rate of 19.2 mg h^{-1} of TTIP under 125 W plasma increases by 14 % to a mode diameter of 1.38 nm compared to 1.21 nm for the condition without plasma (Fig. 3c). Similarly, for negatively charged clusters, the concentration of the flame-generated particles under 125 W plasma increases by 59 % and 265 % for the feed rate of 9.6 and 19.2 mg h^{-1}, respectively, compared to the condition without plasma (Fig. 4b and c). The mode mobility diameter increases by 28 % to 0.81 nm and by 42 % to 1.18 nm for a feed rate of 9.6 and 19.2 mg h^{-1}, respectively, under 125 W plasma compared to the condition without plasma (Fig. 4b and c).

At higher TTIP feed rates of 28.7, 38.4, and 48 mg h^{-1} in the corona-discharge-assisted combustion atmosphere, we observe the Ti-containing particle size shifting towards a smaller size than compared to a flame without plasma. Under 125 W plasma, the mode mobility diameter of the positively charged clusters decreases by 6 % to 3.8 and 4.3 nm for both 38.4 mg h^{-1} (Fig. 3e) and 48 mg h^{-1} (Fig. 3f) TTIP feed rates but remained unchanged at 2.63 nm for the 28.7 mg h^{-1} (Fig. 3d) TTIP feed rate. The mobility diameter decreases for the negatively charged clusters by 6 %, 9 %, and 12 % to 2.6, 3.8, and 4 nm, respectively (Fig. 4d, e, and f). We also examined the effect of the power of corona discharge on size distribution. We find that promotion and suppressive effects of particle formation and growth remain for plasmas of both powers, but the promotional effects are stronger for a corona discharge with the higher power of 125 W.

Figure 5 shows the size distribution of particles formed using TEOS and the corresponding feed rates. Like the size distribution of particles formed using TTIP, the particles generated show both promotional and suppressive effects on particle growth depending on the precursor feed rate. We also see that the concentration of negatively charged particles in the

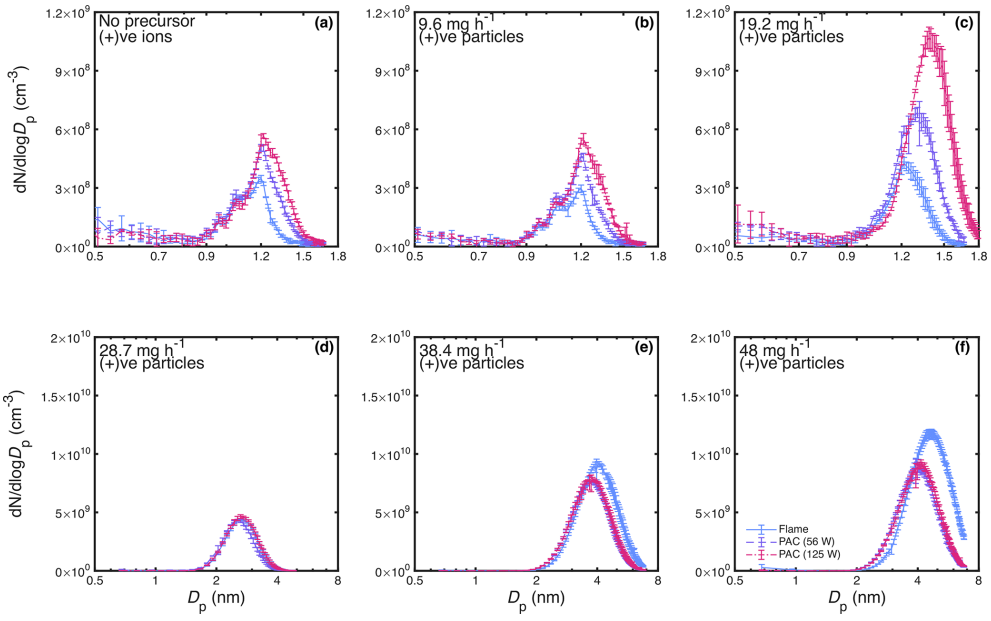

Figure 3. **(a)** The size distribution of positive ions without any TTIP; **(b)**, **(c)**, **(d)**, **(e)**, and **(f)** are the size distributions of positively charged Ti-containing clusters with TTIP feed rates ranging from 9.6 to 48 mg h^{-1}. Each panel compares the influence of corona discharge at a power of 56 and 125 W on the size distribution. Error bars denote the standard deviation.

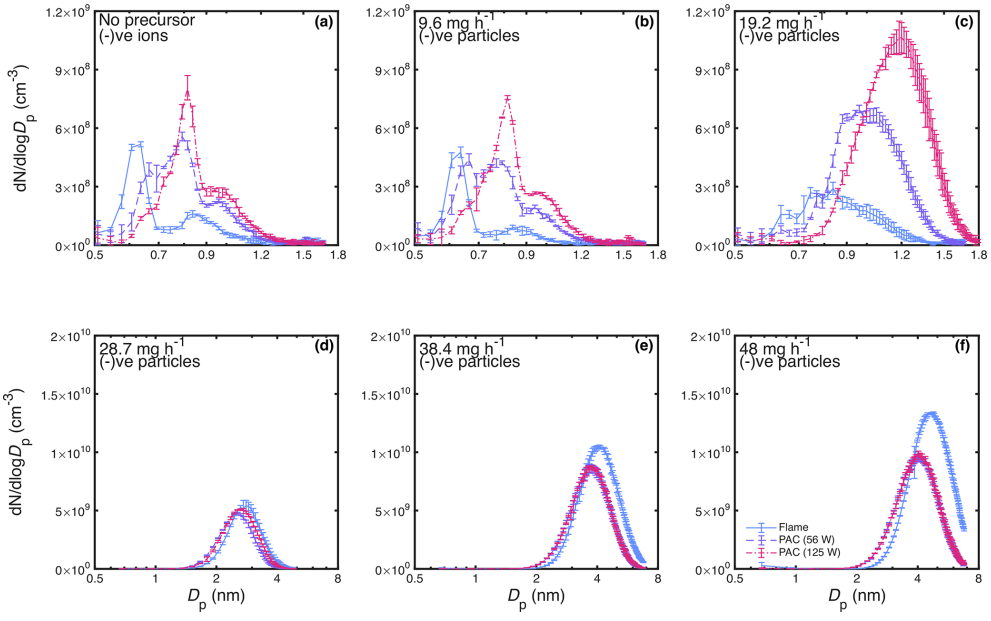

Figure 4. **(a)** The size distribution of negative ions without any TTIP; **(b)**, **(c)**, **(d)**, **(e)**, and **(f)** are the size distributions of negatively charged Ti-containing clusters with TTIP feed rates ranging from 9.6 to 48 mg h^{-1}. Each panel compares the influence of corona discharge at a power of 56 and 125 W on the size distribution. Error bars denote the standard deviation.

flame-only condition for the feed rates of 80 mg h^{-1} (Fig. 5b and e) and 100 mg h^{-1} (Fig. 5c and f) is much lower than that of positively charged particles. Despite electrons being excellent negative-charge carriers, in a flame without plasma, the number of electrons is lower than that of the number of positive ions. This causes more Si-containing particles to be charged positive. Assuming that most of the Si-containing particles are SiO_2 and most of Ti-containing particles are TiO_2, the Si-containing particles have a very low dielectric constant of 3.9 compared to the Ti-containing particles, which have a dielectric constant of 30. As a result, we see a huge concentration difference between the positively and

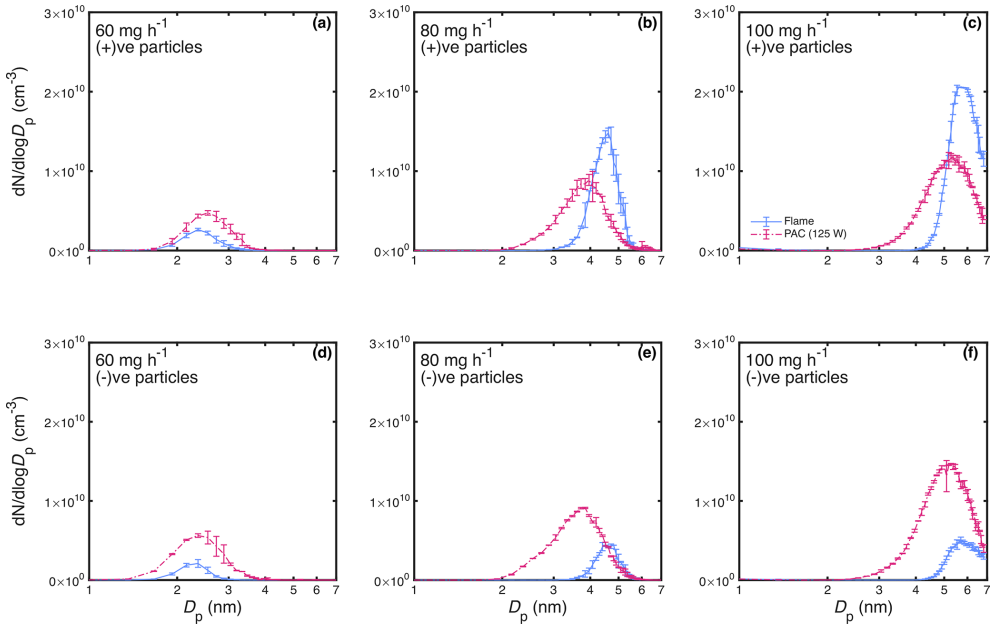

Figure 5. Panels **(a)**, **(b)**, and **(c)** show the size distribution of positively charged Si-containing clusters. Similarly, **(d)**, **(e)**, and **(f)** show the size distribution of negatively charged Si-containing clusters. The size distributions are shown for TEOS feed rates ranging from 60 to 100 mg h^{-1}. Each panel compares the influence of a corona discharge at a power of 125 W on the size distribution. Error bars denote the standard deviation.

negatively charged particles. At a relatively lower feed rate of 60 mg h^{-1}, we observe a higher concentration of particles with corona-discharge-assisted combustion compared to the flame without plasma (Fig. 5a and d). The size of the formed particles also increases due to the presence of the plasma. For the feed rate of 60 mg h^{-1}, we see the mode mobility diameter increase by 8 % to 2.54 nm (Fig. 5a). For higher TEOS feed rates of 80 and 100 mg h^{-1}, we observe the Si-containing particle size of both polarities shifting towards a smaller mode mobility size with corona-discharge-assisted combustion compared to the flame without plasma (Fig. 5b, c, e, and f). The mode mobility diameter of positively charged clusters decreases by 14 % to 4 nm and by 4.5 % to 5.4 nm for 80 mg h^{-1} (Fig. 5b) and 100 mg h^{-1} (Fig. 5c), respectively, in the presence of plasma. Meanwhile, the mode mobility diameter of negatively charged clusters decreases by 20.1 % to 3.85 nm (Fig. 5e) and by 7.5 % to 5.27 nm (Fig. 5f), respectively. Though we saw suppressive effects on mode mobility diameter in Figs. 4 and 5 with both 56 W plasma and 125 W plasma, we did not see the suppressive effects scale with plasma power.

3.3 Mechanism underlying the influence of corona discharge on particle formation

Figure 6 shows the percentage change in modal mobility diameter, which is obtained from the number size distributions shown in Figs. 3 and 4. The modal diameter for each condition corresponds with the diameter which has the highest

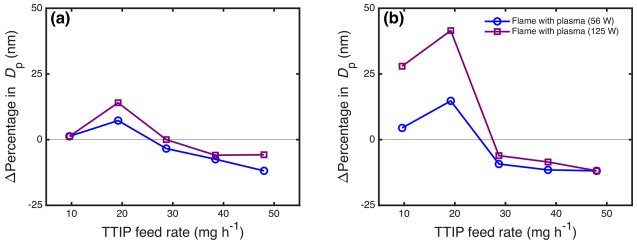

Figure 6. Panels **(a)** and **(b)** show the effects that the corona discharge has on the mode size of positively and negatively charged Ti-containing particles, respectively. In both plots **(a)** and **(b)**, the line at $y = 0$ is the reference to Ti-containing particles generated from non-plasma combustion.

number concentration in the size distribution. From Fig. 6, we can see that when we introduced the high-frequency AC corona discharge in the flame, particle formation and growth were promoted under relatively lower precursor feed rates, ≤ 19.2 mg h^{-1}, but were suppressed under higher precursor feed rates, ≥ 28.7 mg h^{-1}, with respect to the particles generated from non-plasma combustion. The promotion effect under the low precursor feed rates (TTIP feed rates ≤ 19.2 mg h^{-1} and TEOS feed rate ≤ 80 mg h^{-1}) was likely due to the introduction of the plasma-generated ions that had a higher or similar concentration compared to the synthesized particles, which could coagulate and form larger particles. It is also possible that the introduction of the ions leads to ion-induced nucleation, where ions in nucleating vapors

can enhance nucleation rates (Adachi et al., 1992; Lovejoy et al., 2004; Yang et al., 2024). This enhancement has been reported in previous studies on the particle formation kinetics of TiO_2 and SiO_2 particles (Adachi et al., 2004; Wang et al., 2015). Beyond the effect of ions in increasing nucleation rates, the presence of an electron-rich atmosphere has also been shown to promote the formation of particle nuclei at lower supersaturation levels, thereby further enhancing the nucleation rate (Vishnyakov et al., 2011). We start observing the suppression of particle growth at higher TTIP feed rates of 28.7, 38.4, and 48 mg h^{-1} (Fig. 6). A similar trend is seen at higher TEOS feed rates of 80 and 100 mg h^{-1}. In the case of both precursors, the peak mobility diameter decreased in the presence of a corona discharge. We should note that the sampling height is fixed in this work. Therefore, the measurement under different precursor feed rates captures different stages of growth for the nanoparticles. Ion-induced nucleation likely also promoted particle formation at the larger precursor concentration, which occurred before the particles are sampled. The fact that the plasma suppressed particle formation under the higher precursor concentration indicates that the suppression effect is stronger than the promotion effect in particle growth during PAC under higher precursor feed rates.

Here, we further use different models to examine the effect of plasma on aerosol charging. We mainly focus on the suppression effect of the plasma on particle formation and growth under higher precursor feed rates, which is relevant in gas-phase particle synthesis and pollution control, where particles of relatively larger sizes are formed under high precursor feed rates. Due to the high concentration of ions and in PAC atmosphere, the nascent particles are bound to be charged by the charge carriers. Understanding such charging is crucial as it determines inter-particle dynamics in the flame and in the downstream flow region. Particles in PAC and flame systems are mainly charged by collisional mechanisms, where the charge carriers impart charges by colliding with particles.

Figure 7 shows the charge accumulated on the Ti-containing particles due to diffusion, n_{diff}, and field charging effects, n_{fld}, in all operating conditions. The charges accumulated on Si-containing particles are very similar to those accumulated by Ti-containing particles, except for Si-containing particles acquiring less charge from field charging due to their lower dielectric constant of 3.9. The charge accumulated by Si-containing particles is provided in Fig. S1 in the Supplement. By comparing Fig. 7a and b, we can see that with the introduction of a corona discharge, the charges accumulated due to diffusion charging in PAC with plasma of power 125 W are 5.8 % to 53.8 % higher than the charges that are accumulated in the flame-only condition, showing that the diffusion charging is enhanced. On the other hand, the diffusion charging due to the negative ions in the presence of plasma with power 125 W was 15.3 %–38.9 % lower than without the plasma. This is not surprising considering

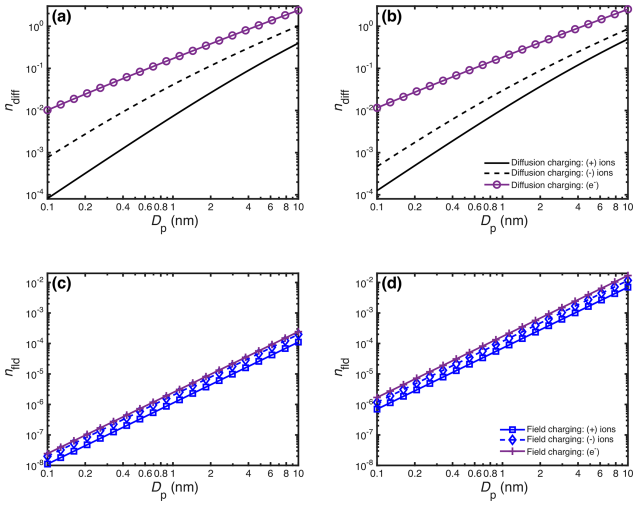

Figure 7. The charge acquired by TiO_2 particles with a dielectric constant of 30. **(a)** Diffusion charging in the flame-only condition. **(b)** Diffusion charging in PAC with a plasma power of 125 W. **(c)** Field charging in the flame-only condition. **(d)** Field charging in PAC with a plasma power of 125 W.

the generation of negative ions with lower mobility in the presence of plasma than in a flame without plasma (Fig. 2b). The enhancement in diffusion charging despite PAC negative ions having less mobility than flame ions is likely due to the greater enhancement of diffusion charging by electrons in PAC. We observe that this phenomenon is stronger with enhancement of 13 %–54 % at a smaller particle size, $D_p = 0.1$ nm, than the enhancement of 5.8 %–25.6 % at a bigger particle size, $D_p = 10$ nm.

Similarly, if we compare Fig. 7c and d for charge accumulated due to field charging by electrons, we see that for the condition with plasma of power 125 W, the charge accumulated is ~ 69 times higher than in the flame-only condition. From Fig. 7, we also see that particles accumulate more negative charge than they do positive charge. Such preferential charging is likely due to the higher mobility and lower mass of negative ions than that of positive ions. Though field charging is significantly enhanced due to the strong electric field in PAC, diffusion charging is still dominant in the observed size range (1–10 nm). Field charging effects become more dominant with the increase in particle size as more field lines intersect with the particle surface.

By introducing corona discharge into the flame, we increase the concentration of electrons. It is important to note that the electrons generated in the corona discharge or the flame have very high mobility and a small size, which cannot be measured by HRDMA. Here, we assume that the number of electrons is the same as the concentration of positive ions and calculate the diffusion and field charging effects of electrons. However, in reality, the electron concentration is likely much higher in plasma-assisted combustion (PAC) than in the flame-only condition. A higher electron concen-

tration results in a greater accumulation of negative charges on particles. From Fig. 7a and b, we can see that the diffusion charging due to electrons is several orders of magnitude greater than that due to positive and negative ions. This higher charging capability is due to their extremely high mobility ($4000\,cm^2\,V^{-1}\,s^{-1}$) (Bisetti and El Morsli, 2012) and low mass (9.11×10^{-31} kg), enabling electrons to diffuse much faster than heavier ions in the considered PAC system. The combined effects of high-diffusion charging by electrons and preferential negative charging of particles will result in a greater fraction of particles being charged negatively. As a result, particle formation and growth of flame-generated particles will be suppressed due to electrostatic repulsion. In industrial applications, the precursor concentrations are in the heavily loaded regime. Based on the results of this study, in the heavily loaded regime, increasing ion concentration to match the precursor concentration should give similar results. This result is also supported by our previous work done on characteristic charging and coagulation time (Wang et al., 2017a). However, it is also possible that the suppression in particle growth by coagulation is due to the reduced residence time of the particle in the post-flame zone. To fully understand the effect of plasma on combustion synthesis of nanomaterials, in situ measurements need to be combined with ex situ imaging and chemical analysis. However, imaging analyses, such as transmission electron microscopy (TEM) and atomic force microscopy (AFM), are challenging at the sub-5 nm size range, as they require the capture and analysis of highly diffusive particles. Similar challenges arise when one tries to sample particles for chemical analysis (Botero et al., 2016; Commodo et al., 2019; Fang et al., 2014; Schulz et al., 2019; Veronesi et al., 2022). Therefore, future work is needed to understand the influence of plasma on particle formation and growth via more comprehensive techniques.

4 Conclusions

In this study, we introduced a corona discharge in a flame using a high-voltage AC power source. Upon scanning the ion size distributions using HRDMA, we found out that we are not generating significant quantities of new ionic species; we are only increasing the concentration of the existing flame ions. Though we do not see any significant changes to the mobility diameter for the positive ions, we do see a shift in the size distribution relating to the negative ions. We also examined the effect of corona discharge on particle formation by studying the effect on size distribution of particles when we introduce synthesis precursors (TTIP and TEOS) to the flame. From our results we found that the effect of corona discharge on particle formation depends on the synthesis precursor concentration. Particle formation and growth were promoted under low precursor feed rates but suppressed under higher precursor feed rates. The promotion effect under low precursor feed rates was likely due to the introduction of the plasma-generated ions that have a higher or similar concentration compared to the synthesized particles, which can coagulate and form larger particles. It is also possible that the introduction of the ions leads to ion-induced nucleation, where ions in nucleating vapors can enhance nucleation rates. The suppression effect of the corona discharge on particle formation and growth is likely due to the high diffusion charging due to electrons and preferential negative charging of particles due to the higher mobility of the negative ions. Based on the results of this study, for industrial applications in the heavily loaded regime, increasing ion concentration to match the precursor concentration should give similar results. We also observe that in corona-discharge-assisted combustion, field charging is greatly enhanced. The findings of this study help us understand the effect of plasmas on particles during combustion synthesis of nanoparticles and pollution control using PAC. We should note that mobility analysis alone is insufficient to fully resolve plasma effects on particle formation; complementary offline imaging and chemical characterization of newly formed particles would clarify mechanistic insight and improve the control of particle formation in PAC.

Appendix A: Nomenclature

a	Particle radius, m
c	Mean thermal speed of ions, $m\,s^{-1}$
d	Distance between the discharge electrodes, 6×10^{-3} m
E_0	Intensity of applied electric field, $V\,m^{-1}$
k	Boltzmann's constant, $1.38 \times 10^{-23}\,J\,K^{-1}$
n_{diff}	Charge acquired by the particle due to diffusion charging, number of elementary units
n_{fld}	Charge acquired by the particle due to field charging, number of elementary units
n_s	Saturation charge of the particle, number of elementary units
N	Concentration of ions, ions m^{-3}
N_0	Concentration of ions at a large distance from particle, ions m^{-3}
t	Time, s
T	Absolute temperature, °K
Z	Electrical mobility, $m^2\,V^{-1}\,s^{-1}$
ϵ	Elementary unit of charge, 1.602×10^{-19} C

Data availability. The data associated with this article are available at https://doi.org/10.5281/zenodo.19796408 (Bagya Ramesh et al., 2026). Additional raw data can be made available by the corresponding author upon request.

Supplement. The supplement related to this article is available online at https://doi.org/10.5194/ar-4-265-2026-supplement.

Author contributions. Chanakya Bagya Ramesh: investigation, data curation, formal analysis, writing – original draft, methodology, visualization. Frank Daoru Han: writing – review and editing, supervision. Yang Wang: conceptualization, funding acquisition, supervision, writing – review and editing.

Competing interests. The contact author has declared that none of the authors has any competing interests.

Disclaimer. Publisher's note: Copernicus Publications remains neutral with regard to jurisdictional claims made in the text, published maps, institutional affiliations, or any other geographical representation in this paper. The authors bear the ultimate responsibility for providing appropriate place names. Views expressed in the text are those of the authors and do not necessarily reflect the views of the publisher.

Financial support. This research has been supported by the National Science Foundation Directorate for Engineering (grant no. 2132655).

Review statement. This paper was edited by Georgios Kelesidis and reviewed by three anonymous referees.

References

Adachi, M., Okuyama, K., and Seinfeld, J. H.: Experimental studies of ion-induced nucleation, J. Aerosol Sci., 23, 327–337, 1992.

Adachi, M., Kusumi, M., and Tsukui, S.: Ion-induced nucleation in nanoparticle synthesis by ionization chemical vapor deposition, Aerosol Sci. Technol., 38, 496–505, https://doi.org/10.1080/02786820490460734, 2004.

Alavi, M., Hamblin, M., Mozafari, M., Rose Alencar de Menezes, I., and Douglas Melo Coutinho, H.: Surface modification of SiO2 nanoparticles for bacterial decontaminations of blood products, Cellular, Molecular and Biomedical Reports, 2, 87–97, https://doi.org/10.55705/cmbr.2022.338888.1039, 2022.

Altendorfner, F., Kuhl, J., Zigan, L., and Leipertz, A.: Study of the influence of electric fields on flames using planar LIF and PIV techniques, P. Combust. Inst., 33, 3195–3201, https://doi.org/10.1016/j.proci.2010.05.112, 2011.

Bagya Ramesh, C. and Wang, Y.: Ions Generated from a Premixed Methane-Air Flame: Mobility Size Distributions and Charging Characteristics, Combust. Sci. Technol., 196, 4041–4056, https://doi.org/10.1080/00102202.2023.2203818, 2024.

Bagya Ramesh, C., Han, F. D., and Wang, Y.: Nascent Titanium/Silicon-Containing Particle Formation in Corona Discharge Assisted Combustion, Zenodo [data set], https://doi.org/10.5281/zenodo.19796408, 2026.

Belhi, M., Domingo, P., and Vervisch, P.: Direct numerical simulation of the effect of an electric field on flame stability, Combust. Flame, 157, 2286–2297, https://doi.org/10.1016/j.combustflame.2010.07.007, 2010.

Bisetti, F. and El Morsli, M.: Calculation and analysis of the mobility and diffusion coefficient of thermal electrons in methane/air premixed flames, Combust. Flame, 159, 3518–3521, https://doi.org/10.1016/j.combustflame.2012.08.002, 2012.

Botero, M. L., Adkins, E. M., González-Calera, S., Miller, H., and Kraft, M.: PAH structure analysis of soot in a non-premixed flame using high-resolution transmission electron microscopy and optical band gap analysis, Combust. Flame, 164, 250–258, https://doi.org/10.1016/j.combustflame.2015.11.022, 2016.

Bradley, D. and Nasser, S. H.: Electrical Coronas and Burner Flame Stability, Combust. Flame, 55, 53–58, https://doi.org/10.1016/0010-2180(84)90148-2, 1984.

Braun, J. H., Baidins, A., and Marganski, R. E.: TiO_2 pigment technology: a review, Prog. Org. Coat., 20, 105–138, https://doi.org/10.1016/0033-0655(92)80001-D, 1992.

Carbone, F., Barone, A. C., De Filippo, A., Beretta, F., D'Anna, A., and D'Alessio, A.: Coagulation and Adhesion of Nanoparticles generated in flame from droplets of Nickel Nitrate aqueous solutions, Chem. Eng. Trans., 16, 87–94, 2008.

Carbone, F., Canagaratna, M. R., Lambe, A. T., Jayne, J. T., Worsnop, D. R., and Gomez, A.: Detection of weakly bound clusters in incipiently sooting flames via ion seeded dilution and collision charging for (APi-TOF) mass spectrometry analysis, Fuel, 289, 119820, https://doi.org/10.1016/j.fuel.2020.119820, 2021.

Cha, M. S., Lee, S. M., Kim, K. T., and Chung, S. H.: Soot suppression by nonthermal plasma in coflow jet diffusion flames using a dielectric barrier discharge, Combust. Flame, 141, 438–447, https://doi.org/10.1016/j.combustflame.2005.02.002, 2005.

Commodo, M., Kaiser, K., De Falco, G., Minutolo, P., Schulz, F., D'Anna, A., and Gross, L.: On the early stages of soot formation: Molecular structure elucidation by high-resolution atomic force microscopy, Combust. Flame, 205, 154–164, https://doi.org/10.1016/j.combustflame.2019.03.042, 2019.

De Giorgi, M. G., Ficarella, A., Sciolti, A., Pescini, E., Campilongo, S., and Di Lecce, G.: Improvement of lean flame stability of inverse methane/air diffusion flame by using coaxial dielectric plasma discharge actuators, Energy, 126, 689–706, https://doi.org/10.1016/j.energy.2017.03.048, 2017.

Ehn, A., Petersson, P., Zhu, J. J., Li, Z. S., Aldén, M., Nilsson, E. J. K., Larfeldt, J., Larsson, A., Hurtig, T., Zettervall, N., and Fureby, C.: Investigations of microwave stimulation of a turbulent low-swirl flame, P. Combust. Inst., 36, 4121–4128, https://doi.org/10.1016/j.proci.2016.06.164, 2017.

Fang, J., Wang, Y., Attoui, M., Chadha, T. S., Ray, J. R., Wang, W. N., Jun, Y. S., and Biswas, P.: Measurement of Sub-2 nm clusters of pristine and composite metal oxides during nanomaterial synthesis in flame aerosol reactors, Anal. Chem., 86, 7523–7529, https://doi.org/10.1021/ac5012816, 2014.

Fernández de la Mora, J. and Kozlowski, J.: Hand-held differential mobility analyzers of high resolution for 1–30 nm particles: Design and fabrication considerations, J. Aerosol Sci., 57, 45–53, https://doi.org/10.1016/j.jaerosci.2012.10.009, 2013.

Fialkov, A. B.: Investigations on ions in flames, Prog. Energy Combust. Sci., 23, 399–528, https://doi.org/10.1016/s0360-1285(97)00016-6, 1997.

Friedlander, S. K.: Smoke, Dust, and Haze: Fundamentals of Aerosol Behavior, Oxford University Press, New York, ISBN 9780195129991, 2000.

Galley, D., Pilla, G., Lacoste, D., Ducruix, S., Lacas, F., Veynante, D., and Laux, C. O.: Plasma-Enhanced Combustion of a Lean Premixed Air-Propane Turbulent Flame using a Nanosecond Repetitively Pulsed Plasma, in: 43rd AIAA Aerospace Sciences Meeting and Exhibit, 1193, https://doi.org/10.2514/6.2005-1193, 2005.

Gan, Y., Luo, Y., Wang, M., Shi, Y., and Yan, Y.: Effect of alternating electric fields on the behaviour of small-scale laminar diffusion flames, Appl. Therm. Eng., 89, 306–315, https://doi.org/10.1016/j.applthermaleng.2015.06.041, 2015.

Gröhn, A. J., Pratsinis, S. E., Sánchez-Ferrer, A., Mezzenga, R., and Wegner, K.: Scale-up of nanoparticle synthesis by flame spray pyrolysis: The high-temperature particle residence time, Ind. Eng. Chem. Res., 53, 10734–10742, https://doi.org/10.1021/ie501709s, 2014.

Jang, H. D.: Generation of silica nanoparticles from tetraethylorthosilicate (TEOS) vapor in a diffusion flame, Aerosol Sci. Technol., 30, 477–488, https://doi.org/10.1080/027868299304516, 1999.

Ju, Y. and Sun, W.: Plasma assisted combustion: Dynamics and chemistry, Prog. Energy Combust. Sci., 48, 21–83, https://doi.org/10.1016/j.pecs.2014.12.002, 2015a.

Ju, Y. and Sun, W.: Plasma assisted combustion: Progress, challenges, and opportunities, Combust. Flame, 162, 529–532, https://doi.org/10.1016/j.combustflame.2015.01.017, 2015b.

Kammler, H. K., Jossen, R., Morrison, P. W., Pratsinis, S. E., and Beaucage, G.: The effect of external electric fields during flame synthesis of titania, Powder Technol., 135–136, 310–320, https://doi.org/10.1016/j.powtec.2003.08.023, 2003.

Kim, S. K., Chang, H., Cho, K., Kil, D. S., Cho, S. W., Jang, H. D., Choi, J. W., and Choi, J.: Enhanced photocatalytic property of nanoporous TiO2/SiO 2 micro-particles prepared by aerosol assisted co-assembly of nanoparticles, Mater. Lett., 65, 3330–3332, https://doi.org/10.1016/j.matlet.2011.02.028, 2011.

Larriba, C., Hogan, C. J., Attoui, M., Borrajo, R., Garcia, J. F., and De La Mora, J. F.: The mobility-volume relationship below 3.0 nm examined by tandem mobility-mass measurement, Aerosol Sci. Technol., 45, 453–467, https://doi.org/10.1080/02786826.2010.546820, 2011.

Li, S., Ren, Y., Biswas, P., and Tse, S. D.: Flame aerosol synthesis of nanostructured materials and functional devices: Processing, modeling, and diagnostics, Prog. Energy Combust. Sci., 55, 1–59, https://doi.org/10.1016/j.pecs.2016.04.002, 2016.

Li, Y. H., Chen, C. T., and Fang, H. K.: Effects of a microwave-induced corona discharge plasma on premixed methane-air flames, Energy, 188, 116007, https://doi.org/10.1016/j.energy.2019.116007, 2019.

Liao, Y. H. and Zhao, X. H.: Plasma-Assisted Stabilization of Lifted Non-premixed Jet Flames, Energy and Fuels, 32, 3967–3974, https://doi.org/10.1021/acs.energyfuels.7b03940, 2018.

Liu, B. Y. H. and Yeh, H.-C.: On the Theory of Charging of Aerosol Particles in an Electric Field, J. Appl. Phys., 39, 1396–1402, https://doi.org/10.1016/0021-9797(69)90368-3, 1968.

Lovejoy, E. R., Curtius, J., and Froyd, K. D.: Atmospheric ion-induced nucleation of sulfuric acid and water, J. Geophys. Res.-Atmos., 109, D08204, https://doi.org/10.1029/2003JD004460, 2004.

Mäkelä, J. M., Jokinen, V., Mattila, T., Ukkonen, A., and Keskinen, J.: Mobility distribution of acetone cluster ions, J. Aerosol Sci., 27, 175–190, https://doi.org/10.1016/0021-8502(95)00560-9, 1996.

Nanomaterials Market Size And Share Report, https://www.grandviewresearch.com/industry-analysis/nanotechnology-and-nanomaterials-market (last access: 22 June 2025), 2025.

Niu, F., Li, S., Zong, Y., and Yao, Q.: Catalytic behavior of flame-made Pd/TiO_2 nanoparticles in methane oxidation at low temperatures, J. Phys. Chem. C, 118, 19165–19171, https://doi.org/10.1021/jp504859d, 2014.

Ohisa, H., Kimura, I., and Horisawa, H.: Control of Soot Emission of a Turbulent Diffusion Flame by DC or AC Corona Discharges, Combust. Flame, 116, 653–661, 1999.

Pratsinis, S. E.: Flame aerosol synthesis of ceramic powders, Prog. Energy Combust. Sci., 24, 197–219, https://doi.org/10.1016/S0360-1285(97)00028-2, 1998.

Ren, Y., Cui, W., and Li, S.: Electrohydrodynamic instability of premixed flames under manipulations of dc electric fields, Phys. Rev. E, 97, 013103, https://doi.org/10.1103/PhysRevE.97.013103, 2018.

Rittler, A., Deng, L., Wlokas, I., and Kempf, A. M.: Large eddy simulations of nanoparticle synthesis from flame spray pyrolysis, P. Combust. Inst., 36, 1077–1087, https://doi.org/10.1016/j.proci.2016.08.005, 2017.

Rosocha, L. A., Coates, D. M., Platts, D., and Stange, S.: Plasma-enhanced combustion of propane using a silent discharge, Phys. Plasmas, 11, 2950–2956, https://doi.org/10.1063/1.1688788, 2004.

Saito, M., Arai, T., and Arai, M.: Control of Soot Emitted from Acetylene Diffusion Flames by Applying an Electric Field, Combust. Flame, 119, 356–366, 1999.

Schulz, F., Commodo, M., Kaiser, K., De Falco, G., Minutolo, P., Meyer, G., D'Anna, A., and Gross, L.: Insights into incipient soot formation by atomic force microscopy, P. Combust. Inst., 37, 885–892, https://doi.org/10.1016/j.proci.2018.06.100, 2019.

Serrano-Bayona, R., Chu, C., Liu, P., and Roberts, W. L.: Flame Synthesis of Carbon and Metal-Oxide Nanoparticles: Flame Types, Effects of Combustion Parameters on Properties and Measurement Methods, Materials, 16, 1192, https://doi.org/10.3390/ma16031192, 2023.

Siefering, K. L. and Griffin, G. L.: Growth Kinetics of CVD TiO2: Influence of Carrier Gas, J. Electrochem. Soc., 137, 1206–1208, https://doi.org/10.1149/1.2086632, 1990.

Spicer, P. T., Artelt, C., Sanders, S., and Pratsinis, S. E.: Flame synthesis of composite carbon black-fumed silica nanostructured particles, J. Aerosol Sci., 29, 647–659, https://doi.org/10.1016/S0021-8502(97)10023-4, 1998.

Su, H. C., Goyal, H., Clark, L., Kook, S., Hawkes, E., Chan, Q. N., Padala, S., Le, M. K., and Ikeda, Y.: In-Cylinder Soot Reduction Using Microwave Generated Plasma in an Optically Accessible Small-Bore Diesel Engine, SAE Technical Papers, 2018-01-0246, https://doi.org/10.4271/2018-01-0246, 2018.

Tang, Y., Simeni Simeni, M., Yao, Q., and Adamovich, I. V.: Non-premixed counterflow methane flames in DC/AC/NS electric fields, Combust. Flame, 240, 112051, https://doi.org/10.1016/j.combustflame.2022.112051, 2022.

Thimsen, E., Rastgar, N., and Biswas, P.: Nanostructured TiO_2 films with controlled morphology synthesized in a single step process: Performance of dye-sensitized solar cells and

photo watersplitting, J. Phys. Chem. C, 112, 4134–4140, https://doi.org/10.1021/jp710422f, 2008.

Ude, S. and De La Mora, J. F.: Molecular monodisperse mobility and mass standards from electrosprays of tetraalkyl ammonium halides, J. Aerosol Sci., 36, 1224–1237, https://doi.org/10.1016/j.jaerosci.2005.02.009, 2005.

Vemury, S. and Pratsinis, S. E.: Corona-assisted flame synthesis of ultrafine titania particles, Appl. Phys. Lett., 66, 3275–3277, https://doi.org/10.1063/1.113402, 1995.

Veronesi, S., Commodo, M., Basta, L., De Falco, G., Minutolo, P., Kateris, N., Wang, H., D'Anna, A., and Heun, S.: Morphology and electronic properties of incipient soot by scanning tunneling microscopy and spectroscopy, Combust. Flame, 243, 111980, https://doi.org/10.1016/j.combustflame.2021.111980, 2022.

Vincent-Randonnier, A., Larigaldie, S., Magre, P., and Sabel'nikov, V.: Experimental study of a methane diffusion flame under dielectric barrier discharge assistance, IEEE T. Plasma Sci., 35, 223–232, https://doi.org/10.1109/TPS.2007.893249, 2007.

Vishnyakov, V. I., Kiro, S. A., and Ennan, A. A.: Heterogeneous ion-induced nucleation in thermal dusty plasmas, J. Phys. D Appl. Phys., 44, 215201, https://doi.org/10.1088/0022-3727/44/21/215201, 2011.

Wang, Y.: Sub 2 nm Particle Characterization in Systems with Aerosol Formation and Growth, Ph.D. thesis, Washington University in St. Louis, USA, 276 pp., https://doi.org/10.7936/K7BV7F1F, 2017.

Wang, Y., Fang, J., Attoui, M., Chadha, T. S., Wang, W. N., and Biswas, P.: Application of Half Mini DMA for sub 2 nm particle size distribution measurement in an electrospray and a flame aerosol reactor, J. Aerosol Sci., 71, 52–64, https://doi.org/10.1016/j.jaerosci.2014.01.007, 2014.

Wang, Y., Liu, P., Fang, J., Wang, W. N., and Biswas, P.: Kinetics of sub-2 nm TiO_2 particle formation in an aerosol reactor during thermal decomposition of titanium tetraisopropoxide, J. Nanopart. Res., 17, 147, https://doi.org/10.1007/s11051-015-2964-y, 2015.

Wang, Y., Sharma, G., Koh, C., Kumar, V., Chakrabarty, R., and Biswas, P.: Influence of flame-generated ions on the simultaneous charging and coagulation of nanoparticles during combustion, Aerosol Sci. Technol., 51, 833–844, https://doi.org/10.1080/02786826.2017.1304635, 2017a.

Wang, Y., Kangasluoma, J., Attoui, M., Fang, J., Junninen, H., Kulmala, M., Petäjä, T., and Biswas, P.: Observation of incipient particle formation during flame synthesis by tandem differential mobility analysis-mass spectrometry (DMA-MS), P. Combust. Inst., 36, 745–752, https://doi.org/10.1016/j.proci.2016.07.005, 2017b.

Wang, Y., Kangasluoma, J., Attoui, M., Fang, J., Junninen, H., Kulmala, M., Petäjä, T., and Biswas, P.: The high charge fraction of flame-generated particles in the size range below 3 nm measured by enhanced particle detectors, Combust. Flame, 176, 72–80, https://doi.org/10.1016/j.combustflame.2016.10.003, 2017c.

Xiong, G., Kulkarni, A., Dong, Z., Li, S., and Tse, S. D.: Electric-field-assisted stagnation-swirl-flame synthesis of porous nanostructured titanium-dioxide films, P. Combust. Inst., 36, 1065–1075, https://doi.org/10.1016/j.proci.2016.08.079, 2017.

Yang, Y., Chen, H., Li, C., and Wang, P.: Ion induced nucleation of charged droplets enhanced by external electric field, Phys. Plasmas, 31, https://doi.org/10.1063/5.0196881, 2024.

Zhao, B., Yang, Z., Wang, J., Johnston, M. V., and Wang, H.: Analysis of soot nanoparticles in a laminar premixed ethylene flame by scanning mobility particle sizer, Aerosol Sci. Technol., 37, 611–620, https://doi.org/10.1080/02786820300908, 2003.

Zhao, H., Liu, X., and Tse, S. D.: Control of nanoparticle size and agglomeration through electric-field- enhanced flame synthesis, J. Nanopart. Res., 10, 907–923, https://doi.org/10.1007/s11051-007-9330-7, 2008.